energies

MDPI

Article

Injection Order and Outlet-Specific Oil Recovery During Foam Treatment of Heterogeneous Sandstone

Lixin Chen [1], Wenming Wu [2,*], Jie Yao [1], Xida Zhou [2] and Xiaocen Liu [1]

[1] Oil and Gas Production Management Area, PetroChina Tarim Oilfield Company, Korla 841000, China; chenlx-tlm@petrochina.com.cn (L.C.); yaojie-tlm@petrochina.com.cn (J.Y.); lxcen-tlm@petrochina.com.cn (X.L.)
[2] Sanya Offshore Oil and Gas Research Institute, Northeast Petroleum University, Sanya 572025, China; zhouxida111@gmail.com
* Correspondence: wwmlh10126@163.com

Abstract

Equal-dose foam treatments can send oil to different outlets. In a two-path model operated at a 5.14 kPa pressure ceiling, sequential placement recovered 34.94% of initial oil at the original producer, compared with 33.06% for premixing. Reversing the bank order gave the largest two-outlet export (54.96%). The sequential lead over premixing was 1.91 percentage points at a common rate of 1.65 mL/min and 1.89 points with a 30 min shut-in under the reference ceiling. The higher-permeability path supplied the forward gain. Suppressing the mobilizer-induced change in the oil endpoint reversed the ranking. In single- and parallel-core nitrogen floods at 140 °C, recovery increased by 13.64 and 21.95 points from the end of initial gas injection to the end of the chase. Cartesian simulations placed the subsequent gas flow along the flanks of the conductive streak in the single plug and into the lower-permeability plug in the parallel system. In a separate fixed-order simulation of the Donghe 1 well pair, 300 m^3 per active bank gave the largest first-year oil difference per unit of active liquid among five doses. The comparison identifies how bank order changes oil delivery to a producer and how the assumed oil-endpoint response controls the ranking.

Keywords: producer-side treatment; foam mobility control; injection order; nitrogen coreflood; parallel sandstone cores; directional oil recovery

1. Introduction

Gas can reach a production well through a conductive streak while oil remains in adjacent sandstone. Foam reduces gas mobility and changes the pressure gradients that drive later fluids [1,2]. Which paths receive the next bank depends on permeability, gas and liquid saturations, and the formation and decay of foam [3–7]. A producer-side treatment reverses the flow direction during liquid placement, then restores the original direction at gas restart [8–10].

Bank order may therefore change where oil is displaced and where it is produced. A polymer-enhanced foaming bank can prolong foam persistence and raise aqueous viscosity [11]. A subsequent mobilizer bank moves through the saturation and resistance fields established by the preceding liquids. Even at equal dose, the mobilizer can enter different pore volumes and produce different amounts of oil at the gas-production outlet and the opposite boundary.

We test this sequence effect in a two-path axial model by holding component dose and delivered gas volume fixed and comparing sequential placement, premixing and re-

Check for updates

Academic Editor: Shu Tao

Received: 25 October 2026
Revised: 16 November 2026
Accepted: 25 November 2026
Published: 27 November 2026

Copyright: © 2026 by the authors. Licensee MDPI, Basel, Switzerland. This article is an open access article distributed under the terms and conditions of the Creative Commons Attribution (CC BY) license.

versed bank order. Two staged nitrogen corefloods provide measured pressure and recovery histories. Cartesian simulations identify gas redistribution within a single plug and between parallel plugs. The axial model carries the measured geometry into the numerical comparison and isolates the effects of delivery rate, shut-in and the oil endpoint. The Donghe 1 well-pair forecasts address a separate treatment decision, the active-bank volume at fixed order.

2. Experimental and Numerical Design

2.1. Nitrogen Floods and Formulation Measurements

We used two independently jacketed sandstone plugs (Table 1 and Figure 1a). The higher-permeability plug Hc formed the single-core system. Hc and the lower-permeability plug Lc shared the inlet and outlet manifolds in the parallel system. A pump and intermediate vessels delivered liquids, and a separate line supplied nitrogen. We measured differential pressure across the system and collected oil and gas at the outlets. Tests used 140 °C, a reservoir-condition pressure setting of 60 MPa, formation brine at 2.34×10^5 mg/L and a nominal forward nitrogen rate of 0.05 mL/min. The separate jackets confine flow within the plugs, with redistribution through the manifolds.

Table 1. Sandstone properties measured for the floods and pore volumes used in the axial fit.

Plug	Role	Length (mm)	Diameter (mm)	Porosity (%)	Permeability (mD)	Model PV (mL)
DH1-6-9-12	Hc	55.365	24.785	17.100	6.045	4.568
DH1-H18-5	Lc	46.385	24.680	14.169	1.148	3.147

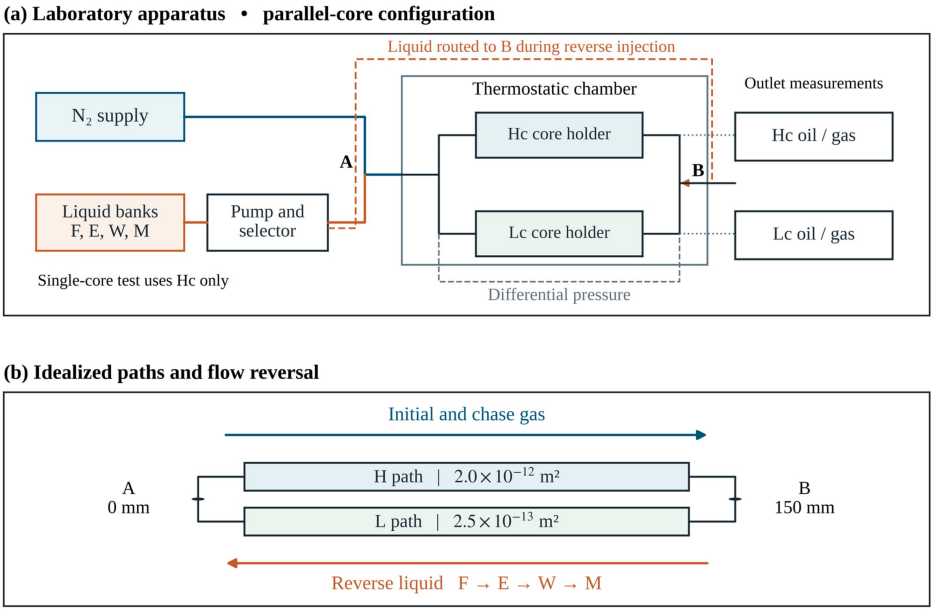


Figure 1. Laboratory flow routing and the two-path calculation. (**a**) Plugs Hc and Lc share end manifolds; the single-core test uses Hc alone. (**b**) The simulated paths carry forward gas from A and reverse treatment from B.

The conventional foaming liquid F contained 0.5 wt% of an APG0810/DAB-35 blend prepared at a 1:1 mass ratio. The enhanced liquid E added 0.2 wt% xanthan gum (XG) to F. W denotes formation brine, and M denotes the 1.5 wt% bio-based surfactant solution used for imbibition. After brine and oil saturation, we injected nitrogen from A until oil production from Hc at B became negligible. We then injected liquid from B. The single-core

treatment used 0.5 pore volume (PV) F and 0.5 PV E. The parallel treatment used 0.5 PV F, 0.5 PV E, 0.1 PV W and 0.5 PV M. The corresponding modeled liquid volumes were 4.57 and 12.34 mL. We closed both ends for 30 min and resumed forward nitrogen injection from A. The cumulative gas volume covers the two forward stages.

We prepared the base foaming solution in formation brine and aged it at 140 °C for 24 h before blending. Table 2 compares the base solution and the xanthan gum (XG) formulation, with nominal XG contents of 0 and 0.2 wt% before dilution. Each sample was mixed at 6000 rpm for 5 min. We recorded the foam volume and the drainage half-life, defined as the time required for half of the liquid initially held in the foam to drain. After the foam had collapsed, a 50 mL aliquot was diluted with an equal volume of formation brine and retested under the same mixing conditions. Surface tension and oil–water interfacial tension were measured for both formulations before and after dilution.

Table 2. Bulk foam and interfacial response to XG. Nominal XG content refers to the solution before brine dilution.

Sample	Nominal XG (wt%)	Foam Volume (mL)	Drainage Half-Life (s)	Surface Tension (mN/m)	Oil–Water IFT (mN/m)
Before dilution	0	525	733	25.79	0.876
Before dilution	0.2	420	4295	26.74	1.162
After dilution	0	455	612	26.53	1.008
After dilution	0.2	380	2263	29.97	1.216

2.2. Spatial Simulations of the Two Laboratory Floods

We simulated the two core arrangements in tNavigator 23.4 (Figure 2a,b). The 5 × 20 × 1 single-core grid represents Hc. In the 11 × 20 × 1 parallel grid, a central inactive strip separates the two plugs, and inactive end cells represent the shorter Lc. Each grid retains its plug length, equivalent cross-sectional area and porosity. A central streak at twice the background permeability provides a preferential gas path in each plug. The grids use reservoir oil–water and gas–oil relative permeability, high-pressure fluid properties and the reservoir pressure reference. The single layer resolves axial and transverse variation within the modeled plane. We extracted oil saturation and axial gas velocity before treatment and after restart.

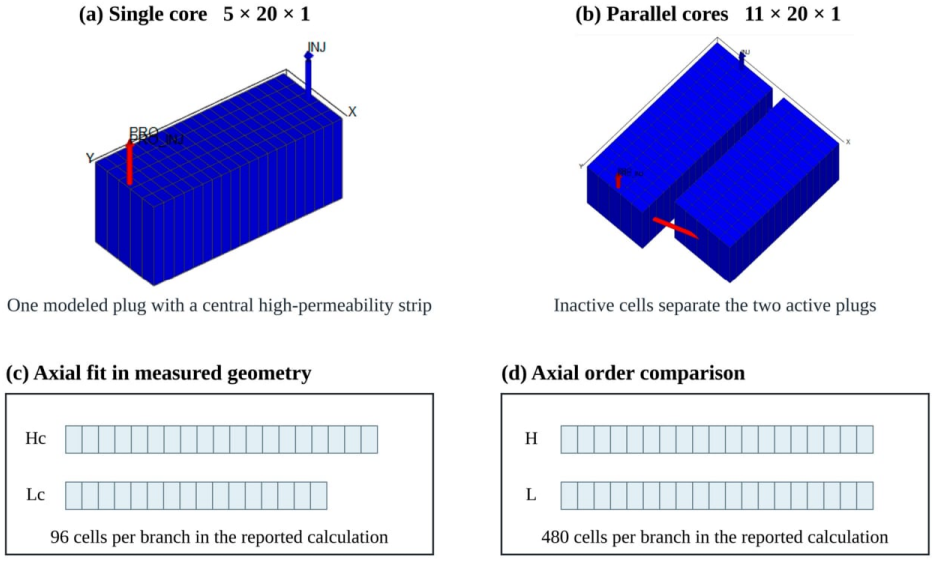


Figure 2. Spatial grids for the single plug (**a**) and parallel cores (**b**), and axial representations of the measured arrangement (**c**) and the equal-size controlled paths (**d**).

2.3. Flow and Chemical Transport Along Parallel Paths

The axial model conserves gas, oil and water volumes in each horizontal path and calculates flow with Darcy's law. Each grid cell carries cross-section-averaged saturations. The immiscible, incompressible phases share one pressure field. The paths share pressures at the end manifolds. The axial calculation omits gravity, explicit capillary pressure gradients and lateral crossflow [12,13].

For each phase, relative permeability is the effective saturation raised to its phase exponent. Effective saturation is the positive saturation above the residual endpoint divided by the mobile pore fraction. The ratio of relative permeability to phase viscosity gives mobility. Water carries the foaming agent, XG and M. The aqueous inventory includes dissolved chemicals and a reversibly retained amount proportional to concentration [14,15]. The foam state represents the local resistance to gas flow [16,17].

Foam forms during flow where the gas, water and foaming agent coexist, with generation slowing as the local foam state approaches its upper limit. The existing foam decays. XG raises water viscosity and slows foam decay. During shut-in, transport and generation stop while the existing foam continues to decay. To obtain gas mobility, we divide the unfoamed value by one plus the product of the foam state, the foam coefficient Fmax and the water-saturation factor fd. This factor is one in the controlled comparison and accounts for foam weakening at low water saturation in the measured plugs [18].

The model uses the highest local concentration of mobilizer M reached in each cell, expressed as a fraction of its stock concentration, to update the residual oil saturation. The endpoint reduction is calculated by multiplying the maximum reduction parameter by the ratio of the peak concentration to the sum of the peak and half-response concentrations. In the reference controlled model, the untreated residual oil saturation is 0.24, the maximum reduction parameter is 0.16, and the half-response concentration is 20% of the stock concentration. At this concentration, the endpoint decreases by 0.08 to 0.16. The model retains the peak-exposure effect through the simulated gas chase as the dissolved M concentration decreases. A zero-reduction case tests how the predicted injection-order ranking depends on this assumption. Cell resistance is calculated by dividing cell length by the product of cross-sectional area, absolute permeability, and total phase mobility. Branch conductance is the reciprocal of the sum of the cell resistances along the branch. In the controlled comparison, the branches share an end-to-end pressure drop, and flow is allocated in proportion to their conductances. If the target rate requires a pressure drop above the prescribed ceiling, the solver reduces the total rate to satisfy that ceiling. A first-order upwind finite-volume scheme updates phase volumes and aqueous chemical inventories [19,20]. The solver then updates the foam state and peak M concentration for use in the next step. Forward recovery counts oil produced at B during both forward gas stages. Reverse export counts oil discharged at A during reverse liquid placement. Both are expressed as percentages of the initial oil volume.

The controlled comparison uses two paths 150 mm long and 38 mm in equivalent diameter, each with porosity 0.16 (Figure 1b). Their combined PV is 54.44 mL. Permeabilities are 2.0×10^{-12} m^2 (H) and 2.5×10^{-13} m^2 (L). Each chemical run delivers 48.99 mL gas at A, 39.20 mL liquid at B and 130.7 mL chase gas at A. Sequential placement is F–E–W–M, the premix uses constant concentrations of two-thirds F stock, one-third XG stock and one-quarter M stock, and the reverse order is M–W–E–F. All three deliver the same volume and amount of each active ingredient (Table 3).

Table 3. Liquid schedules. Component amounts are expressed as the equivalent volume of the prepared stock.

Case	Liquid Order	Foaming Agent (mL Eq.)	XG (mL Eq.)	Mobilizer (mL Eq.)
Carrier	W/W/W/W	0.00	0.00	0.00
Foam only	F/F/W/W	26.13	0.00	0.00
Enhanced without M	F/E/W/W	26.13	13.07	0.00
Mobilizer only	W/W/W/M	0.00	0.00	9.80
Polymer-free	F/F/W/M	26.13	0.00	9.80
Sequential	F/E/W/M	26.13	13.07	9.80
Premixed	F + XG + M in W	26.13	13.07	9.80
Reversed order	M/W/E/F	26.13	13.07	9.80
Enhanced first	E/F/W/M	26.13	13.07	9.80
Spacer last	F/E/M/W	26.13	13.07	9.80

The reference target rate is 1.65 mL/min. Treatment and chase use a 5.14 kPa ceiling, eight times the 0.642 kPa pressure drop at the end of initial gas injection, and a 2.64 min shut-in. To isolate delivery rate, we ran the three orders at 1.65 mL/min under a nonbinding 82.2 kPa ceiling. To isolate shut-in duration, we extended the pause to 30 min under the reference ceiling. The same-gas-volume run continues gas injection without reverse liquid or shut-in. The carrier run retains reversal and shut-in and replaces the active liquids with brine. Table 4 lists the prescribed inputs. At the maximum foam state, the reference resistance coefficient of 80 reduces gas mobility by a factor of 81. At stock XG concentration, the viscosity multiplier is three and the decay-rate multiplier is one-ninth. These controlled calculations prescribe fluid viscosities.

Table 4. Prescribed reference settings for the controlled axial calculation.

Parameter	Reference Value
Initial water, oil and gas saturations	0.28/0.62/0.10
Base water, oil and gas viscosities (mPa·s)	1/4/0.08
Water, untreated oil and gas saturation endpoints	0.12/0.24/0.02
Relative-permeability exponents for water, oil and gas	2/2/2
Foam resistance and water-saturation factor	Fmax = 80; fd = 1
Nominal generation and decay rates (min^{-1})	0.364/0.0182
XG viscosity and stabilization coefficients	$\beta v = 2$; $\beta s = 8$
Reversible storage for foaming agent, XG and mobilizer	0.04/0.10/0.06
Endpoint amplitude and half-response concentration	Am = 0.16; C50 = 0.20
Pressure ceiling (kPa) and shut-in duration (min)	5.14/2.64
Cells per path and time-step coefficient	480 (240 in sweeps); 0.035

2.4. Calibration with the Measured Geometry

The axial fits use the plug lengths, permeabilities and model PVs in Table 1 (Figure 2c). The 24.690 mm diameter used for Lc differs from the measured 24.680 mm by about 0.03% in total pore volume. Hc holds 59.21% of the parallel pore volume and has 4.45 times the single-phase conductance of Lc. The branch and system recoveries imply that Hc held 61.17% of the initial oil. Each fit starts with oil and brine, uses the observed initial gas volume of 8.679 mL for the single core or 15.429 mL for the parallel cores, and applies the experimental 30 min shut-in. The target recovery counts oil through the forward outlet. The calculation records reverse export separately.

Table 5 lists the effective fit parameters. The rate–water-viscosity product sets the pressure scale. In the foam resistance term, an arctangent water-saturation factor has steepness 150 and is centered at the estimated transition saturation. An effective Lc entry-

pressure offset acts during forward gas flow in the parallel fit. Flowing foam kinetics advance with delivered volume. During shut-in, the local decay rate is 0.01819 min^{-1} divided by one plus eight times the local XG stock fraction. The measured-geometry order runs use the same fitted parameters.

Table 5. Effective parameters estimated from the two coreflood histories. The flowing foam coefficients are applied per total model pore volume delivered.

Parameter	Single Core	Parallel Cores
Initial water saturation, by total pore volume	0.6890	0.7028
Untreated oil endpoint Sor,0	0.0827	0.0951
Oil mobility denominator factor	0.349	0.646
Gas relative-permeability exponent	1.032	1.025
Flowing foam generation coefficient	2.88	19.08
Flowing foam decay coefficient	0.010	0.010
Water saturation at half the wetting factor	0.1431	0.1325
Rate–water-viscosity product (mL·mPa·s/min)	0.762	0.266
Foam resistance coefficient Fmax	80 (fixed)	398
Mobilizer endpoint amplitude Am	—	0.0291
Effective entry pressure offset for Lc (MPa)	—	0.0337

We fit 94 curve markers, using 2 percentage points for recovery and 0.05 MPa for pressure as the residual scales. The parallel fit also uses three branch recovery targets and the Lc first-oil window at 2.15–2.25 gas PV. We compare that window with the model's 1-percentage-point crossing. The search used 48 cells per branch, with refinement at 96 cells and a check at 192. We withheld 46 markers from these same histories to check the fit between fitted points. The estimated coefficients describe effective parameter combinations [21–24].

2.5. Reservoir Model and Dose Comparison

The Donghe 1 CIII simulation uses the reservoir grid and the production history match through December 2024. The forecasts span January 2025 through December 2029. During the treatment month, producer DH1-H5 receives the liquids and gas injection at DH1-H3 stops. One month of shut-in follows. Both wells then resume at their preceding-year average controls. The Cartesian core and reservoir grids share reservoir rock and fluid tables. The reservoir foam model uses concentration, phase saturation and capillary number with adsorption, desorption and decay. The transported mobilizer acts through concentration-dependent interfacial tension and wettability with retention. The axial history-match coefficients apply to the core simulations.

The dose cases hold bank order fixed and vary each active bank from 100 to 500 m^3 in 100 m^3 increments. F contains 1.0 wt% base formulation, E adds 0.2 wt% XG and M contains 1.5 wt% mobilizer. The volume-efficiency metric divides the first 12 months of H5 oil after restart minus its preceding operating year by the combined F, E and M volume. A paired continued-gas scenario compares the treatment and continued-injection trajectories on a common calendar.

3. Results

3.1. Single-Core and Parallel-Core Flow Responses

In Hc alone, gas reached the outlet near 0.70 PV, and oil production nearly stopped at 1.90 PV, with 38.63% recovered. Following reverse F–E placement and shut-in, the second gasflood developed a larger pressure rise, and cumulative recovery reached 52.27% at about 3.70 gas PV (Figure 3a,b). In the Cartesian model, high gas velocity initially follows the central streak. During the chase, the velocity field broadens across the flanks, and the oil

saturation there falls (Figures 4a,b and 5a–d). The Cartesian run ends at 46.77% recovery on its own volume axis.

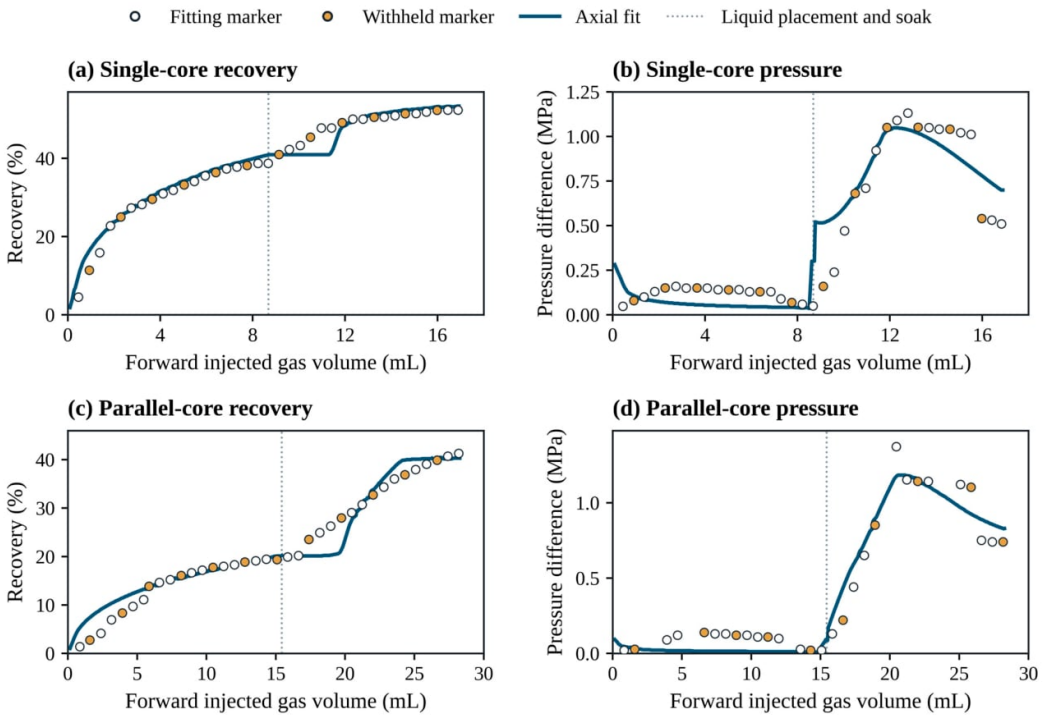


Figure 3. Measured pressure and recovery versus cumulative forward gas volume, with axial fits. Panels (**a**,**b**) show Hc alone and (**c**,**d**) show the parallel system. Filled markers were withheld from fitting. Dotted lines mark the gas volume at which reverse treatment starts.

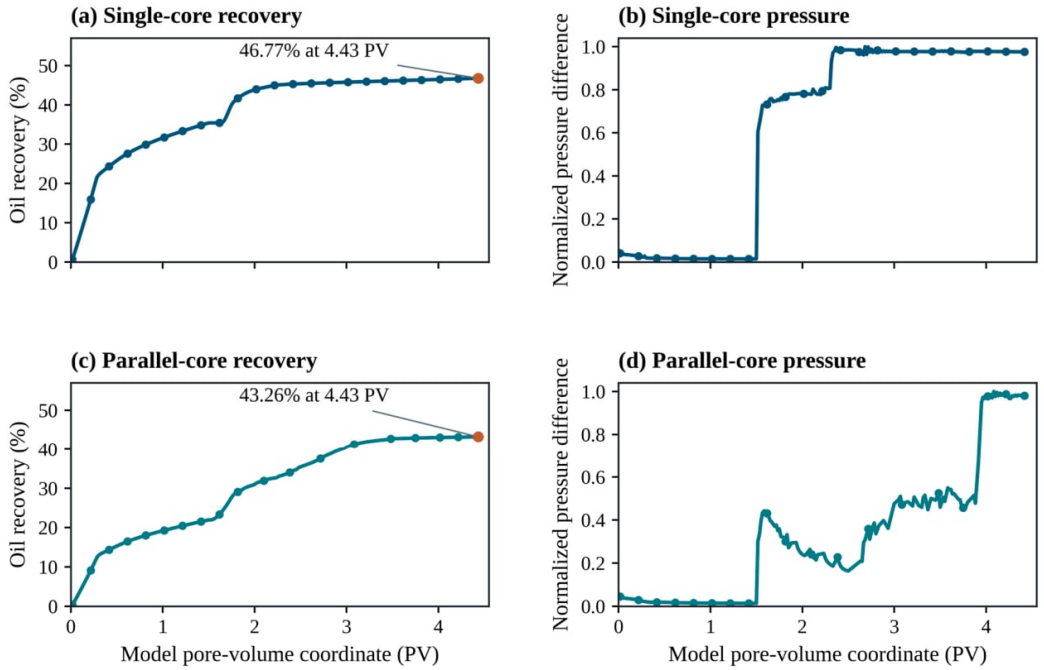


Figure 4. Recovery and pressure histories on the Cartesian simulator volume coordinate. Panels (**a**,**b**) show the single-core run and (**c**,**d**) the parallel-core run. The pressure traces are shown as fractions of the corresponding peak pressure.

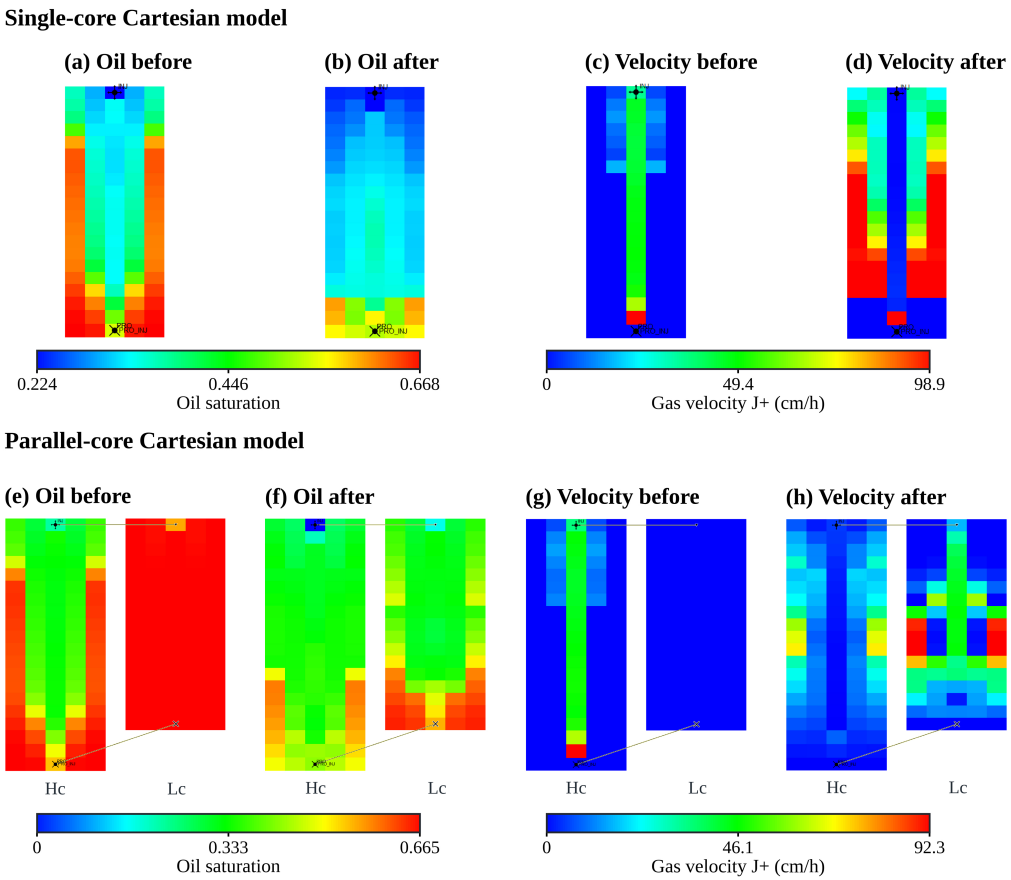


Figure 5. Oil saturation and axial gas velocity before and after treatment. Panels (**a**–**d**) show diversion from the single-core streak toward its flanks; panels (**e**–**h**) show entry into Lc and redistribution within Hc. Forward gas enters from the top of each panel.

In the parallel flood, only Hc produced oil during the initial gas stage, and system recovery reached 19.44%. Following treatment, Lc first produced oil near 2.25 cumulative gas PV and gas near 3.25 PV. The final branch recoveries were 43.18% in Hc and 38.57% in Lc, with 41.39% recovered from the system (Figure 3c,d). The Cartesian velocity field extends from the Hc streak to its flanks and into Lc during the chase, and oil saturation falls in both zones. The parallel Cartesian run reaches 43.26% on the simulator volume axis (Figures 4c,d and 5e–h). The recorded recovery gains of 13.64 and 21.95 percentage points cover reverse placement, shut-in and the gas chase.

3.2. Agreement with the Pressure and Recovery Histories

The Cartesian models locate the gas paths and report recovery on a simulator volume axis. At its endpoint, the parallel calculation gives 43.26%, compared with the measured endpoint of 41.39%. On the displayed converted volume axis, the recovery and pressure RMSEs are 6.57 percentage points and 0.450 MPa. The calculated pressure peaks at 0.853 MPa near 31.50 mL on the converted simulator axis. The experiment peaks at 1.373 MPa and 20.48 mL cumulative gas. We use the axial model to match the histories on the measured gas-volume coordinate.

The axial fit gives 53.23% recovery at 16.88 mL in the single core and 40.34% at 28.18 mL in the parallel cores (Table 6). The parallel pressure maximum is 1.184 MPa at 20.87 mL. The model gives 34.36% recovery in Lc, compared with 38.57% measured. Its 1-percentage-point crossing falls at 17.76 mL, after the observed first-oil window at 16.59–17.36 mL. Arrival and endpoint recovery in Lc place separate constraints on the match.

Table 6. Endpoints of the experiments and two numerical representations. Experimental and axial values share the gas-volume coordinate; the Cartesian values are taken at the simulator endpoint.

Core System	Measured (%)	Axial Fit (%)	Cartesian (%)	Endpoint Volumes
Single core	52.27	53.23	46.77	16.88 mL gas; 4.43 model PV
Parallel cores	41.39	40.34	43.26	28.18 mL gas; 4.43 model PV

Across the markers withheld from the two fitted histories, the recovery RMSEs are 2.06 and 2.92 percentage points. The pressure RMSEs are 0.140 and 0.110 MPa (Table 7). Refining from 96 to 192 cells changes the fitted single-core and parallel-core endpoints by 0.05 and 0.31 percentage points, respectively. The Lc endpoint discrepancy exceeds the observed refinement effect.

Table 7. Root-mean-square errors of the axial pressure and recovery fits at the measured gas volumes.

Response	Fit	Withheld	All	Unit
Single-core recovery	2.51	2.06	2.37	pp
Single-core pressure	0.119	0.140	0.126	MPa
Parallel-core recovery	2.36	2.92	2.56	pp
Parallel-core pressure	0.105	0.110	0.107	MPa

3.3. Recovery and Export at Matched Chemical Dose

At the reference pressure ceiling, sequential placement recovers 34.94% at B, premixing 33.06% and reversed order 32.92% (Figure 6 and Table 8). At A, the same cases expel 14.24%, 18.30% and 22.04% during placement. The reversed case therefore leads the combined outlet total at 54.96%. In the fitted parallel-core geometry at a permeability ratio of 5.27, the corresponding modeled recoveries at B are 40.34%, 36.92% and 34.79%. Both numerical geometries give the same forward ordering among the three cases.

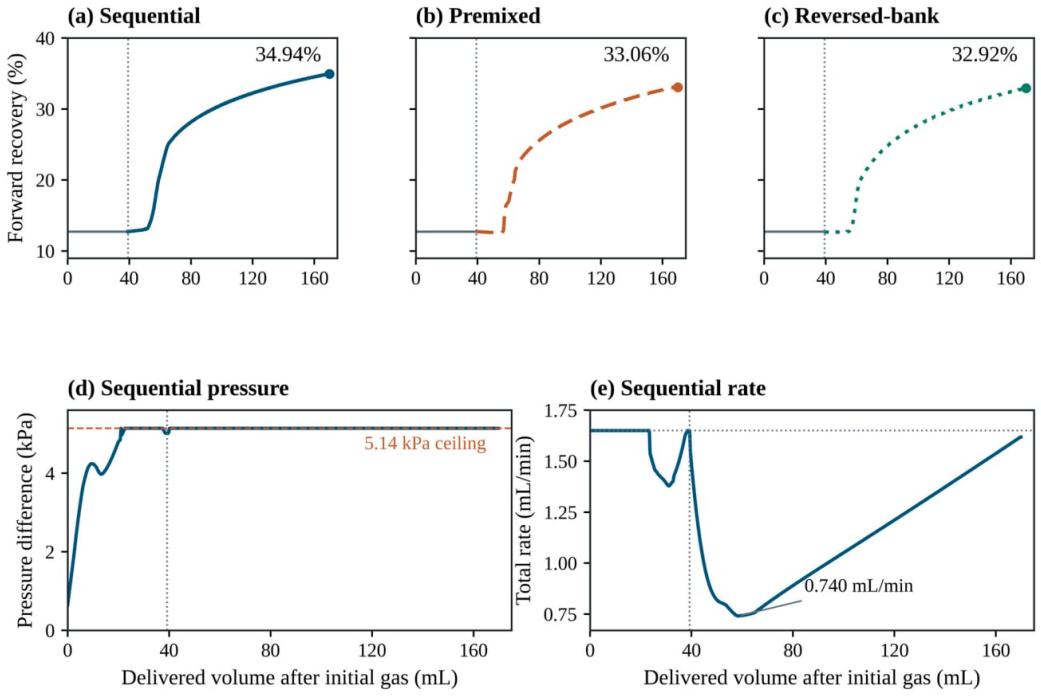


Figure 6. Equal-dose calculations at the reference pressure limit. Panels (**a**–**c**) show oil recovery through B. Panels (**d**,**e**) show pressure and delivered rate for sequential placement. Dotted lines mark the end of reverse liquid placement.

Table 8. Order comparisons at the reference limit, at equal delivery rate, and with a longer shut-in. Recovery and total export use the same initial oil denominator.

Order	Forward at 5.14 kPa (%)	Total at 5.14 kPa (%)	Forward at 1.65 mL/min (%)	Total at 1.65 mL/min (%)	Forward After 30 min Shut-in (%)
Sequential	34.94	49.18	35.14	49.37	34.92
Premixed	33.06	51.36	33.23	51.52	33.03
Reversed	32.92	54.96	33.02	55.06	32.91

The capped and fixed-rate cases in the middle columns use 2.64 min shut-in. The last column uses the 5.14 kPa ceiling and a 30 min shut-in. The fixed-rate cases take 135.27 min from the start of gas injection, including shut-in.

When sequential chase reaches the pressure ceiling, the rate declines to 0.740 mL/min at its minimum. At the same conductance, a rate of 1.65 mL/min would require 11.5 kPa (Figure 6d,e). The capped runs last 179.3, 173.4 and 168.2 min for sequential placement, premixing and reversed order. At a common delivery rate, all three last 135.27 min and recover 35.14%, 33.23% and 33.02% at B. The sequential–premix gap is 1.91 percentage points. At the reference ceiling, extending shut-in to 30 min changes forward recovery by 0.01–0.03 points across the three orders, leaving a 1.89-point sequential lead over premixing.

At matched delivered gas volume, continuing gas without reverse liquid or shut-in recovers 20.20% at B in the controlled model. The brine-carrier run, which preserves reversal and shut-in, gives 12.74% at B and 9.75% at A. The standard sequence delivers 14.74 percentage points more oil at B than uninterrupted gas and 22.20 points more than reverse brine at the reference settings. The two differences quantify the modeled treatment package and the effect of active liquids with the same reversal schedule, respectively. At fixed stage volumes, foam alone, enhanced foam without M, and M alone recover 33.36%, 29.75% and 16.19% at B. Moving W to the end gives 36.43%, above the forward value for F–E–W–M.

3.4. Location of the Forward-Recovery Gain

After sequential placement and shut-in, mean local gas-resistance multipliers are 65.1 in H and 12.9 in L, corresponding to foam states of 0.801 and 0.149. Chase gas encounters retained foaming agent in H and strengthens resistance. By the end of the chase, the mean foam state is 0.989 in H and 0.027 in L. Greater resistance in H diverts flow toward L even at a low local foam state in L (Figure 7).

Sequential placement sends 9.60% of applied M into L, against 9.03% for premixing (Figures 8 and 9b). At 20% of stock M, the prescribed endpoint falls from 0.24 to 0.16. The intervals reaching that concentration extend 8.13 mm under sequential placement and 26.25 mm under premixing. Their centers are 146.4 and 135.5 mm from A. The sequential case concentrates M near B, while premixing exposes a longer part of L to the prescribed endpoint shift.

At the end of sequential placement, the 9.80 mL stock-equivalent M inventory consists of 9.02 mL dissolved and 0.78 mL reversibly stored, with negligible export. Almost all M has exited by the end of the chase, while 4.79 mL foaming agent and 6.43 mL XG remain in stock-equivalent units. The peak-exposure law then retains the reduced oil endpoint in exposed cells. The largest solute-balance residual in the nine original diagnostic cases is 5.34×10^{-12} mL stock equivalent.

The forward gain comes from H. Sequential placement recovers 42.98% of H's initial oil at B, compared with 38.41% for premixing. In L the values are 26.91% and 27.71%. Weighting by equal initial oil volumes gives contributions of +2.28 and −0.40 percentage points to the system difference. Differences in reverse export at A explain the change in ranking when both outlets are counted (Figure 9c,d).

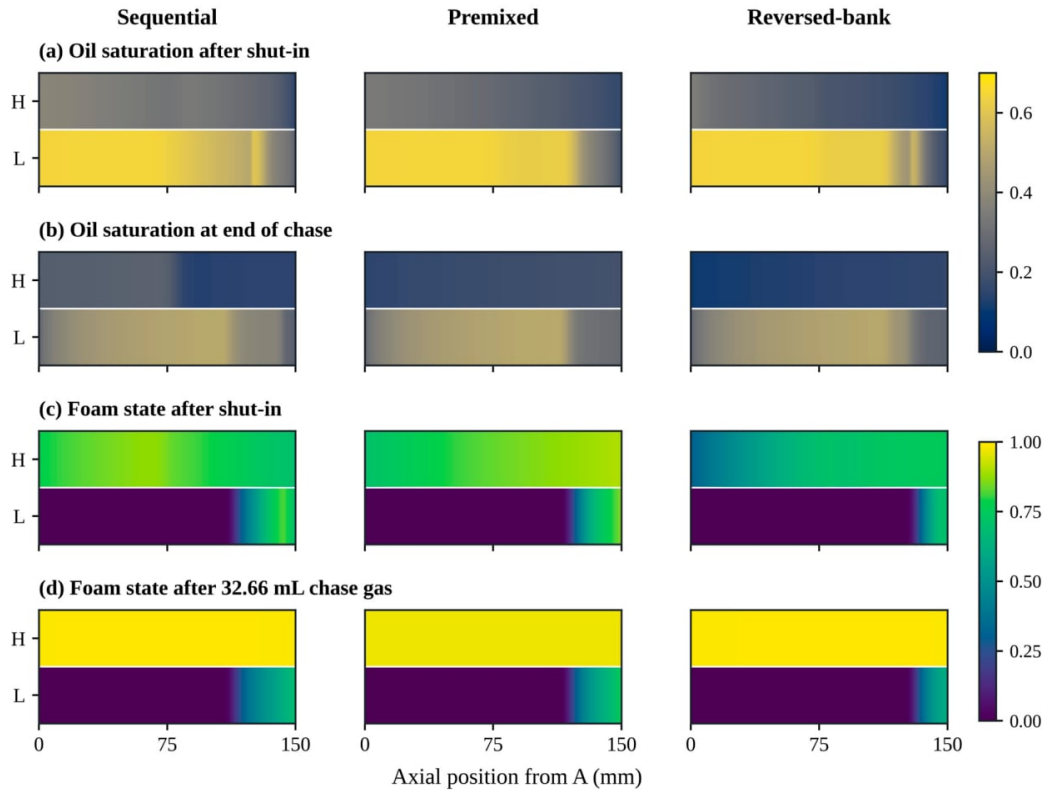


Figure 7. Oil saturation and foam state in H and L. The comparisons show the post-soak and chase states indicated by the panel titles.

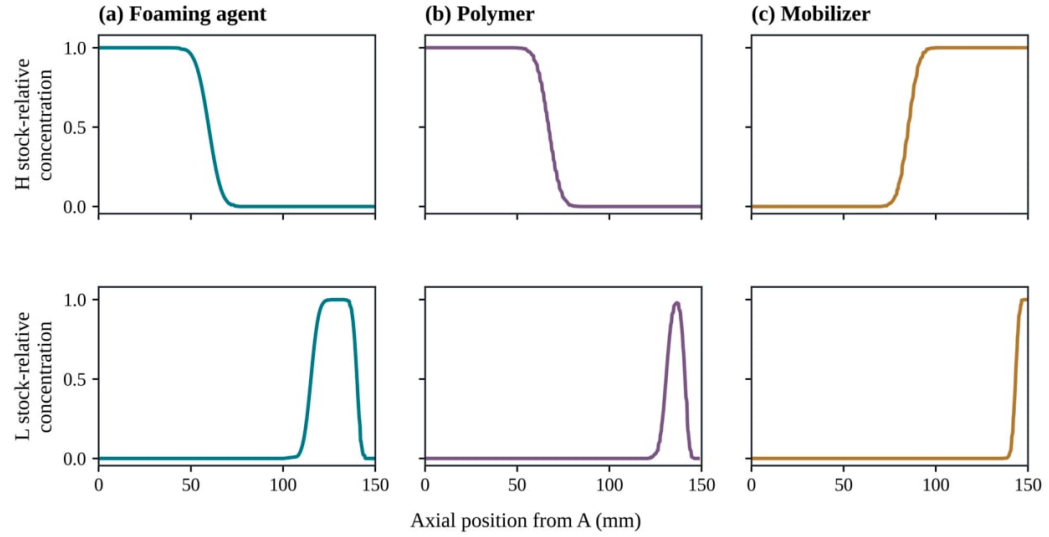


Figure 8. Foaming-agent, polymer and M concentration profiles following shut-in for the sequential case. Each concentration uses its corresponding prepared stock as the reference.

3.5. Sensitivity to Oil Mobilization and Polymer Coupling

The sequential–premix gap spans 1.60–4.08 percentage points over permeability ratios of 2–32 with 240 cells per path. At ratio eight, it falls from 2.06 points on 240 cells to 1.88 on 480 and about 1.8 on 960. Halving and doubling the time-step coefficient change the sequential value by +0.006 and −0.010 points. The phase-volume residual stays below 2.9×10^{-10} mL across 188 reference and sensitivity cases. The added fixed-rate and longer-soak runs satisfy the same phase and chemical balance tolerance.

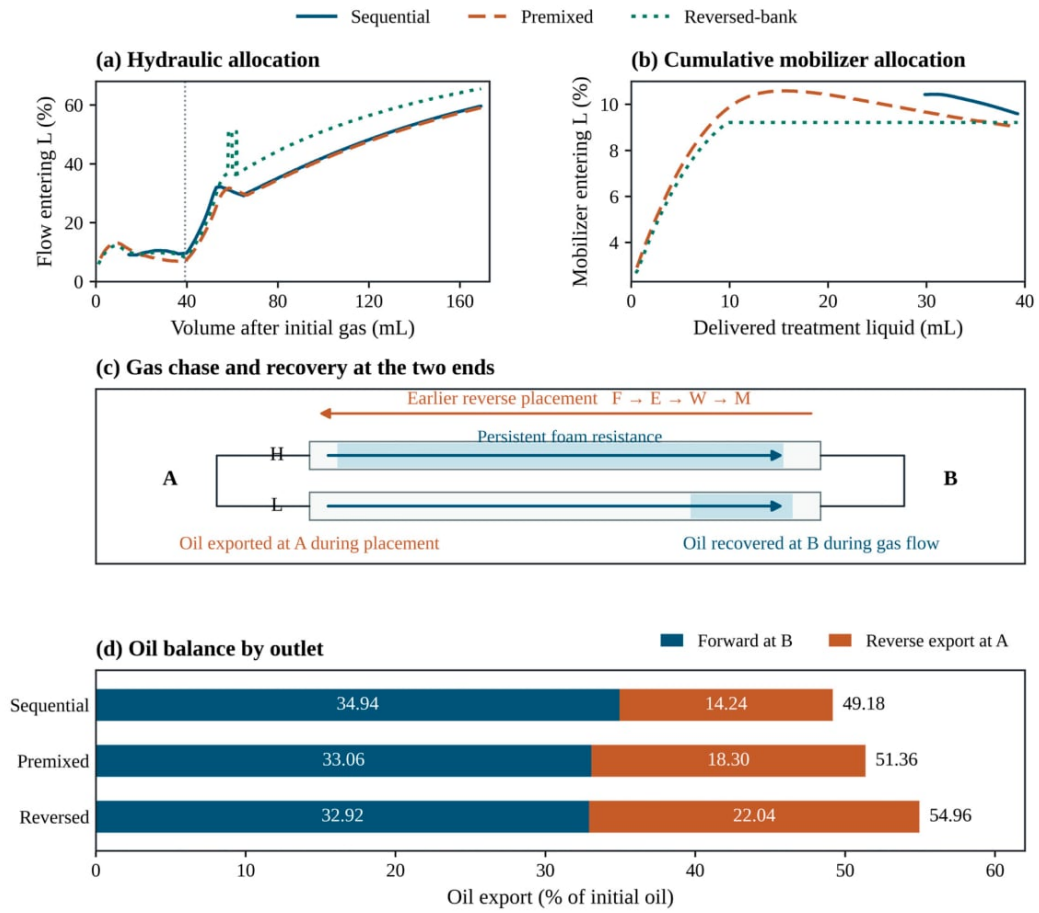


Figure 9. Flow and oil allocation in the controlled paths. (**a**) Instantaneous flow share of L and (**b**) cumulative M dose share of L. (**c**) Flow directions during placement and chase. (**d**) Recovery at B and oil export at A on a common initial-oil basis.

The oil-endpoint response changes the order ranking. Premixing leads by 0.84 percentage points when M leaves the endpoint unchanged (Figure 10b). For maximum endpoint drops of 0.08, 0.16 and 0.20, sequential placement leads by 0.34–0.62, 1.51–2.06 and 2.09–2.77 points, respectively, over the tested half-response concentrations. The H contribution changes from −0.87 points with an unchanged endpoint to +3.26 points when the maximum drop and half-response concentration are both 0.20. In the latter run, L contributes −0.48 points. The response in H controls the sign of the difference.

Adding 0.2 wt% XG increased the undiluted drainage half-life from 733 to 4295 s and reduced foam volume from 525 to 420 mL in the bulk screen. In the axial model, stabilization raises forward recovery from 34.71% to 34.94% at the reference viscosity coupling. Keeping stabilization and removing viscosity coupling raises it to 39.04% (Table 9). Disabling both couplings gives 38.78%, as does omitting XG. At the common rate of 1.65 mL/min, the XG-free case recovers 38.86% and the coupled sequence 35.14%. The modeled difference therefore persists at equal delivery time and reflects changes in aqueous mobility and chemical placement. With the measured parallel-core geometry and fixed fitted coefficients, the XG-free case gives 44.62% forward recovery compared with 40.34% for the staged sequence.

Figure 11 shows the constitutive responses at fixed local conditions. At the mean post-soak foam state in H, a cell retains 1.54% of unfoamed gas mobility under the reference foam coefficient (Figure 11a). With local composition fixed during a 30 min shut-in, 57.9% of the foam state remains without XG and 94.1% at stock XG concentration (Figure 11c). The full shut-in runs in Table 8 also account for the redistribution of fluids and resumption of foam generation during the chase.

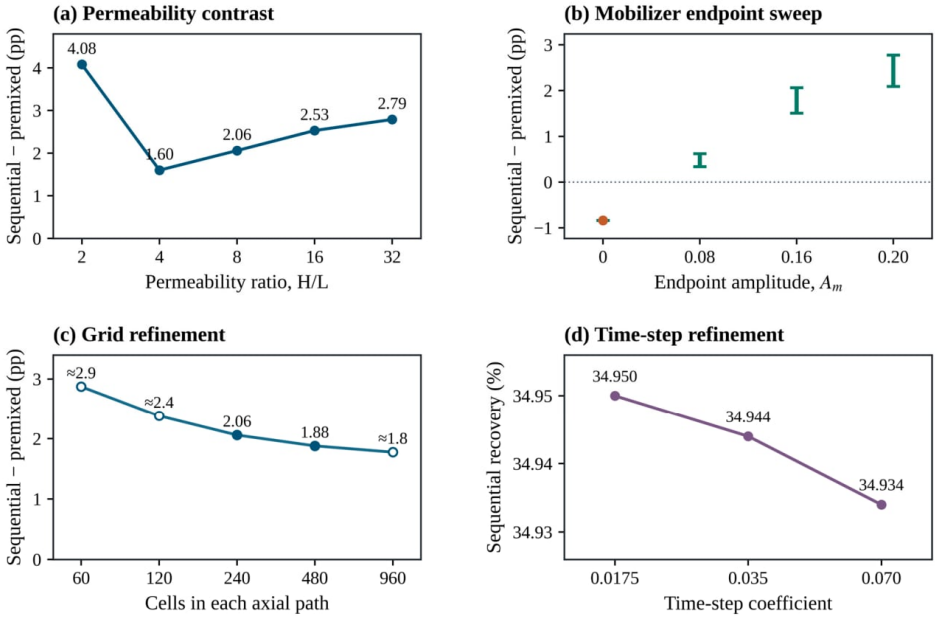


Figure 10. Effect of permeability contrast (**a**), mobilizer endpoint parameters (**b**), grid resolution (**c**), and the time-step coefficient (**d**) on recovery. In (**b**), the horizontal dotted line indicates zero difference in recovery, and the orange point represents the case without mobilizer-induced residual oil saturation reduction (Am = 0) and bars span the tested C50 settings.

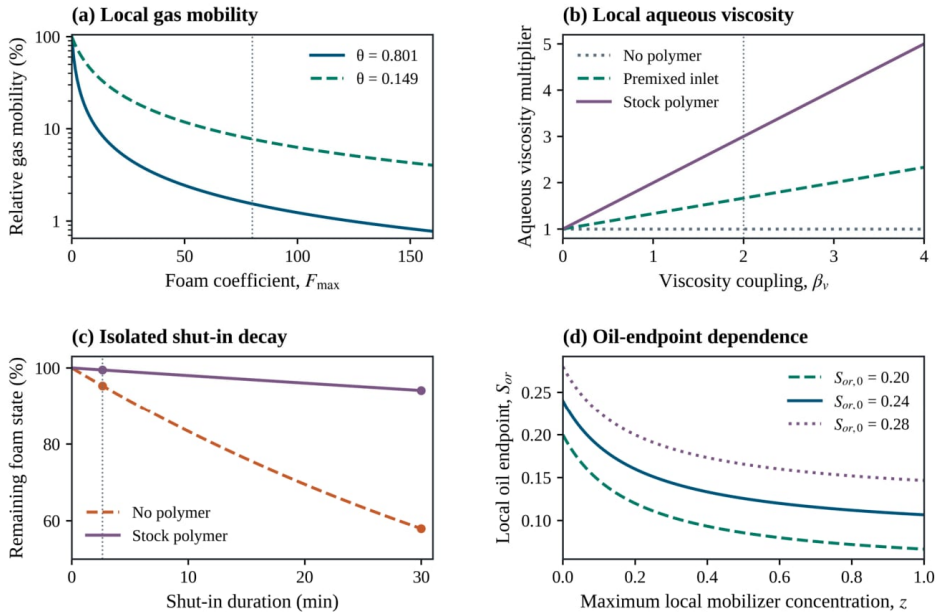


Figure 11. Local response of gas mobility, aqueous viscosity, shut-in foam retention, and the oil endpoint. The panels isolate the stated local conditions from changing flow and placement.

Table 9. Controlled effects of polymer viscosity and foam stabilization.

Case	βv	βs	Forward (%)	Min. Rate (mL/min)	Time (min)	Work (J)
Full coupling	2	8	34.94	0.740	179.3	0.842
Viscosity only	2	0	34.71	0.770	175.6	0.842
Stabilization only	0	8	39.04	0.801	169.1	0.798
Passive polymer	0	0	38.78	0.838	165.6	0.797
Polymer-free	—	—	38.78	0.838	165.6	0.797

3.6. Flow Redistribution and Dose Response in the Well Pair

Before treatment, the simulated streamlines from DH1-H3 cluster near the heel of DH1-H5, where gas inflow is concentrated. After restart, the principal bundle shifts toward the distal completion (Figure 12). Gas still occupies some cells on the original route. The remaining-oil and saturation maps show the corresponding sweep extension toward the toe and oil depletion in parts of the upper and middle intervals (Figure 13).

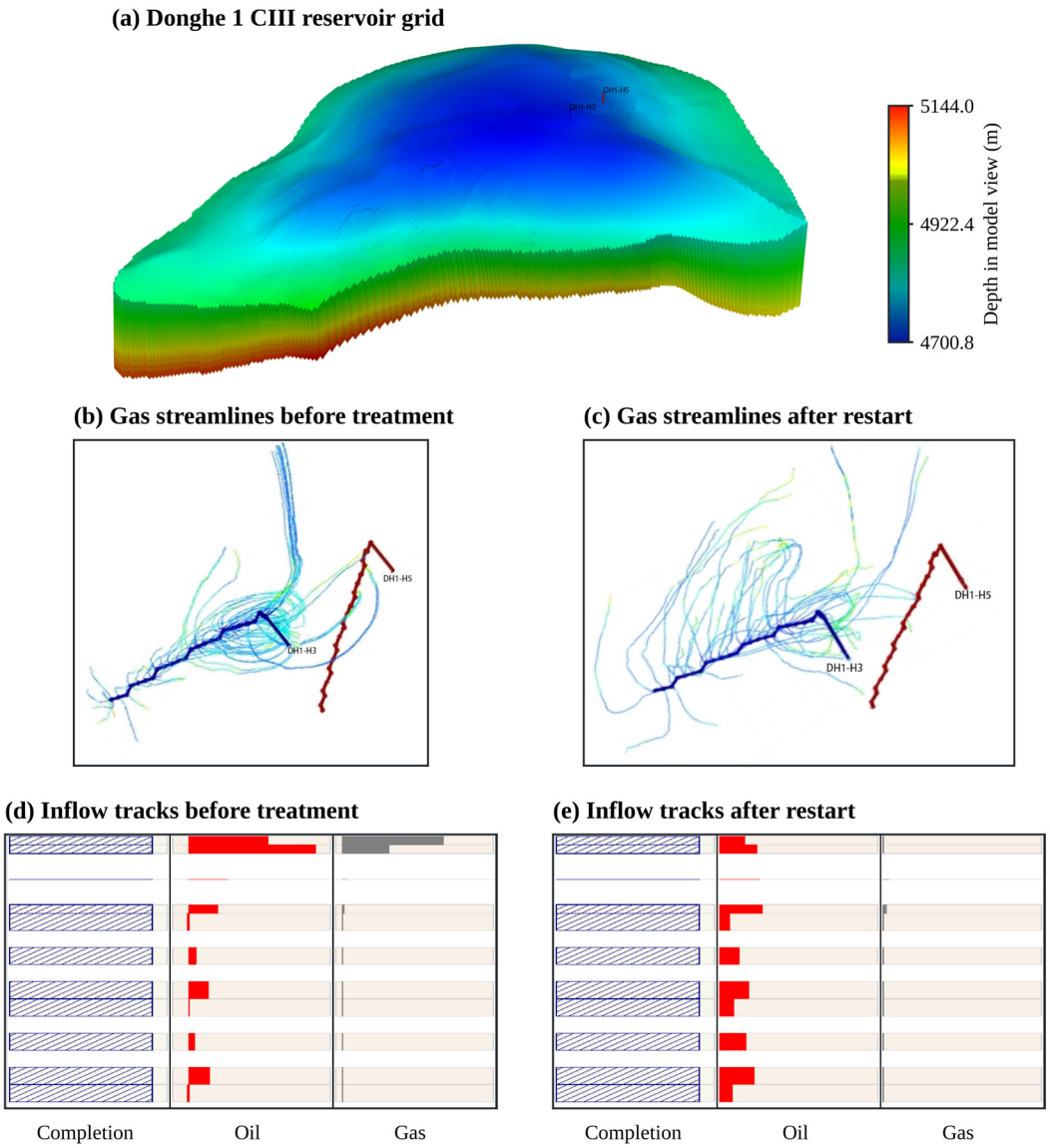


Figure 12. Donghe 1 CIII grid, streamline views and modeled completion inflows. Blue and red trajectories indicate DH1-H3 and DH1-H5. Inflow tracks identify locations of oil and gas entry on each snapshot's display scale.

The staged treatment scenario gives a lower gas–oil ratio and higher oil rate than continued gas injection over the shared forecast interval (Figure 14). The dose series uses a different reference, the preceding operating year. Across 100, 200, 300, 400 and 500 m^3 per bank, the first-year oil differences are 172, 564, 1253, 1368 and 1427 m^3. Volume efficiency peaks at 300 m^3 per bank (1253 m^3 per 900 m^3 of active liquid, or 1.392 m^3/m^3). Adding 100 m^3 per bank beyond 300 m^3 increases the oil difference by 115 m^3, and the following step adds 59 m^3 (Figure 15). The 500 m^3 case gives the largest absolute oil difference.

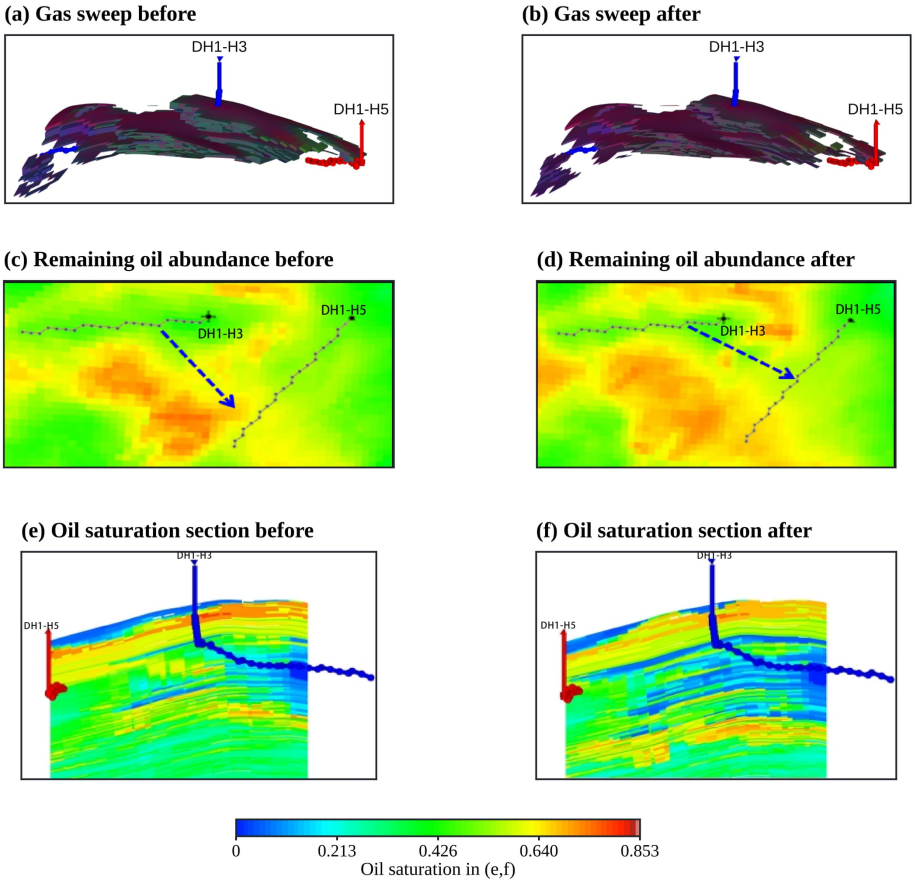


Figure 13. Before-and-after comparison of phase occupancy (**a**,**b**), remaining oil abundance and sweep direction (**c**,**d**), and oil saturation on a common section scale (**e**,**f**). Red, blue and green label gas, water and oil in the phase views.

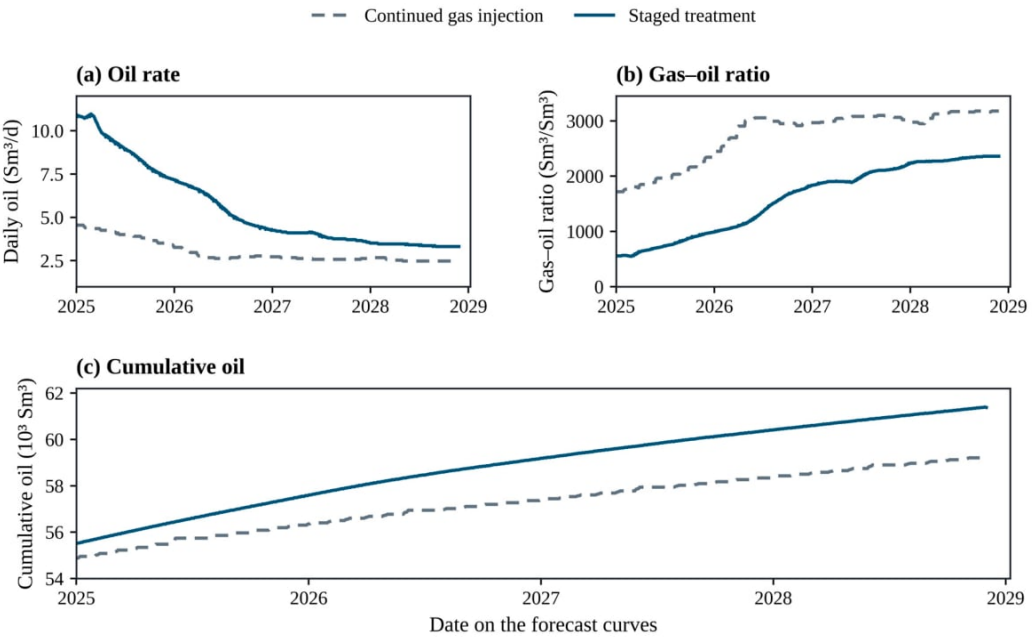


Figure 14. Predicted oil rate, gas–oil ratio and cumulative oil for staged treatment and continued gas on the common forecast calendar.

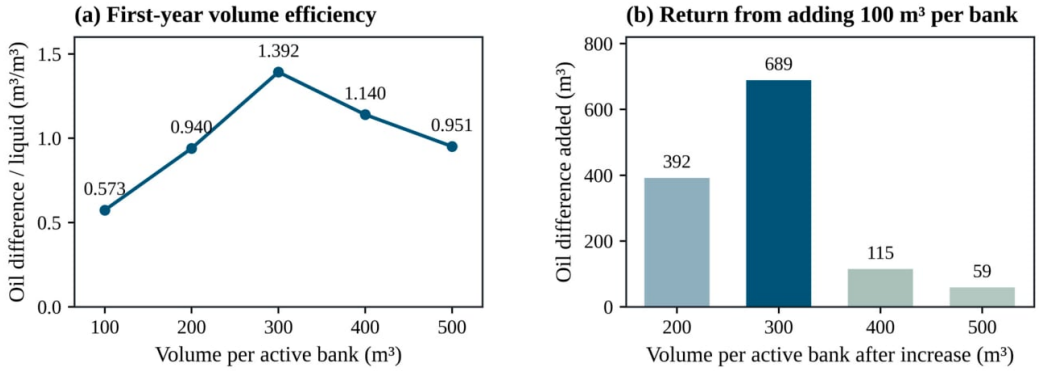


Figure 15. First-year oil difference per combined active-liquid volume (**a**) and marginal oil difference for each additional 100 m^3 per bank (**b**). The baseline is the year before shut-in.

4. Discussion

4.1. Flow Diversion and Oil Production at the Two Ends

The production metric follows the outlet that receives the oil. In H, sequential placement recovers more at B while expelling 24.81% of initial oil at A and leaving 32.22% in the path. Premixing expels 33.30% at A and leaves 28.29%. B-side recovery includes initial gas production, which is common to the modeled orders. The difference at B thus measures their relative delivery to the producing end on restart. In the reservoir, H3 is closed during treatment, and H5 produces after restart. Oil driven away from H5 during placement contributes to production if resumed flow brings it to an active completion.

4.2. Operating Controls and Chemical Response

The order contrast survives matching rate and time and extending the modeled shut-in to 30 min. During shut-in, the local foam state decays while the model holds peak M exposure fixed. A physical soak also allows chemical contact and imbibition. Interfacial tension and viscosity affect oil mobilization during contact [25]. A treated-versus-carrier measurement after a matched flush would constrain how much of the oil-endpoint change lasts over the chase. The observed XG drainage response constrains bulk stability. Rheology at matched temperature and salinity and compatibility during common delivery would constrain the separate viscosity and premix responses.

The fit characterizes displacement and resistance in one staged experiment per geometry. Both fitted foam-decay coefficients lie at the lower search limit, and the parallel foam-resistance estimate is at the upper limit. Gas velocity, saturation and entry pressure all influence foam generation [26–28], and local mobility measurements could help identify their effects [29]. Predictions with the fitted coefficients held fixed across independent premixed and XG-free floods would test whether the model transfers across schedules. Uninterrupted-gas and reverse-brine floods at matched gas volume would distinguish continued displacement from the effect of the staged chemical package and the reversal procedure.

4.3. From Rock Geometry to the Well-Pair Forecast

The idealized paths use about 2026 and 253 mD, compared with 6.045 and 1.148 mD in the plugs. At comparable mobility and geometry, lower permeability raises the pressure drop required for a given rate. Under rate clipping, it also changes delivered volume per time and thus chemical contact. The contrast sweep tests the relative permeabilities of the paths, while the fitted parallel-core geometry represents the measured pair. The well simulation uses reservoir property tables and well controls and holds order fixed. Its

streamline shift shows the modeled redistribution around the completion. The 1253 m^3 historical-year difference describes volume efficiency. A treatment-attributable dose ranking calls for a same-calendar continued-gas reference for every dose. An economic ranking additionally requires chemical, pumping and shut-in costs.

5. Conclusions

1. In the equal-dose axial model, sequential placement gave 1.88 percentage points more forward recovery than premixing at the reference pressure ceiling and 1.91 points more at an equal rate. The gain came from H and changed sign when M left the oil endpoint fixed. Reversing the bank order exported the most oil through the two outlets combined (54.96%).
2. The two staged nitrogen corefloods recorded 13.64- and 21.95-point recovery increases across liquid treatment, shut-in and the gas chase. Cartesian simulations resolved diversion to both streak flanks in the single plug and into Lc in the parallel pair. The axial fits gave recovery RMSEs of 2.06 and 2.92 points on withheld markers from the same experimental histories.
3. In the controlled model, the viscosity penalty of XG exceeds its stabilization benefit at the reference couplings. The fixed-order Donghe 1 forecasts shift gas inflow away from the producer heel. Among five simulated doses, 300 m^3 per bank gives the greatest first-year difference in oil per active liquid volume, 1.392 m^3/m^3 against the preceding operating year.

Author Contributions: Conceptualization, L.C. and W.W.; methodology, L.C., W.W. and X.Z.; software and numerical simulations, X.Z.; validation and formal analysis, L.C., J.Y. and X.Z.; investigation, L.C., J.Y., X.Z. and X.L.; resources and supervision, W.W.; data curation, L.C., W.W. and J.Y.; writing—original draft, L.C., X.Z. and X.L.; writing—review and editing, L.C., W.W. and X.Z.; visualization, X.L. All authors have read and agreed to the published version of the manuscript.

Funding: This research received no external funding.

Data Availability Statement: The experimental measurements and numerical data supporting this study are available from the corresponding author upon reasonable request.

Acknowledgments: The authors would like to express their sincere appreciation to the colleagues who provided valuable discussions, technical assistance, and constructive suggestions during the experimental investigations, numerical simulations, and preparation of this manuscript.

Conflicts of Interest: Lixin Chen, Jie Yao and Xiaocen Liu are affiliated with the Oil and Gas Production Management Area, PetroChina Tarim Oilfield Company. The remaining authors declare no commercial or financial relationships that could be construed as potential conflicts of interest.

References

1. Johnson, P.; Starov, V.; Trybala, A. Foam flow through porous media. *Curr. Opin. Colloid Interface Sci.* **2022**, *58*, 101555. [CrossRef]
2. Moradpour, N.; Yang, J.; Tsai, P.A. Liquid foam: Fundamentals, rheology, and applications of foam displacement in porous structures. *Curr. Opin. Colloid Interface Sci.* **2024**, *74*, 101845. [CrossRef]
3. Ibrahim, K.Z.; Adebayo, A.R.; Isah, A.; Muhammed, N.S. A literature review of strength and stability of foam and their relationship with the absolute permeability of porous media. *J. Pet. Sci. Eng.* **2022**, *211*, 110195. [CrossRef]
4. Zhao, J.; He, Y.; Yang, J. Experimental and population balance model interpretation of foam physics in porous media. *Front. Phys.* **2022**, *10*, 1028414. [CrossRef]
5. Cedro, J.B.; de Paula, F.F.; Chapiro, G. On the modeling of the foam dynamics in heterogeneous porous media. *Adv. Water Resour.* **2025**, *196*, 104882. [CrossRef]
6. Gong, J.K.; Wang, Y.; Kamarul Bahrim, R.Z.B.; Tewari, R.D.; Mahamad Amir, M.I.; Farajzadeh, R.; Rossen, W. Liquid injectivity in a SAG foam process: Effect of permeability. *Pet. Sci.* **2024**, *21*, 302–314. [CrossRef]

7. Ding, M.C.; Li, Q.; Yuan, Y.J.; Wang, Y.F.; Zhao, N.; Han, Y.G. Permeability and heterogeneity adaptability of surfactant-alternating-gas foam for recovering oil from low-permeability reservoirs. *Pet. Sci.* **2022**, *19*, 1185–1197. [CrossRef]
8. de Paula, F.F.; Igreja, I.; Quinelato, T.; Chapiro, G. A numerical investigation into the influence of the surfactant injection technique on the foam flow in heterogeneous porous media. *Adv. Water Resour.* **2023**, *171*, 104358. [CrossRef]
9. Torres-Ulloa, C.; Grassia, P. Foam Propagation with Flow Reversal. *Transp. Porous Media* **2023**, *147*, 629–651. [CrossRef]
10. Grassia, P.; Torres-Ulloa, C.; Shokri, N.; Aryana, S. Pressure-driven growth with forward and reverse foam flow: Modelling foam flow in geological formations. *Proc. R. Soc. A Math. Phys. Eng. Sci.* **2025**, *481*, 20250042. [CrossRef]
11. Wu, Q.; Ding, L.; Zhang, L.; Ge, J.; Rahman, M.A.; Economou, I.G.; Guérillot, D. Polymer enhanced foam for improving oil recovery in oil-wet carbonate reservoirs: A proof of concept and insights into the polymer-surfactant interactions. *Energy* **2023**, *264*, 126256. [CrossRef]
12. Tang, J.; Castañeda, P.; Marchesin, D.; Rossen, W.R. New insights from three-phase fractional-flow modeling of foam-oil displacements in porous media. *Geoenergy Sci. Eng.* **2025**, *255*, 214091. [CrossRef]
13. Castrillón Vásquez, A.J.; Paz, P.Z.S.; Chapiro, G. On the Viscous Crossflow During the Foam Displacement in Two-Layered Porous Media. *Transp. Porous Media* **2024**, *151*, 2835–2857. [CrossRef]
14. Fritis, G.C.; Paz, P.S.; Lozano, L.F.; Chapiro, G. On the Riemann Problem for the Foam Displacement in Porous Media with Linear Adsorption. *SIAM J. Appl. Math.* **2024**, *84*, 581–601. [CrossRef]
15. de Paula, F.F.; Igreja, I.; Quinelato, T.O.; Chapiro, G. Numerical simulation of foam displacement impacted by kinetic and equilibrium surfactant adsorption. *Adv. Water Resour.* **2024**, *188*, 104690. [CrossRef]
16. Grassia, P.; Rajabi, H.; Rosario, R.; Torres-Ulloa, C. Surfactant transport upon foam films moving through porous media. *Colloids Surf. A Physicochem. Eng. Asp.* **2023**, *679*, 132575. [CrossRef]
17. de Miranda, G.B.; Ribeiro, A.d.M.; Chapiro, G.; dos Santos, R.W.; Rocha, B.M. Modeling foam flow in porous media influenced by oil: A computational framework for improved parameter estimation. *Geoenergy Sci. Eng.* **2026**, *258*, 214349. [CrossRef]
18. Hematpur, H.; Hosseini, S.; Mahmood, S.M.; Abdollahi, R.; Hamdi, Z.; Ghamarpoor, R. A new approach to foam flooding modelling with novel parameter estimation techniques. *Sci. Rep.* **2025**, *15*, 22829. [CrossRef] [PubMed]
19. da Silva Pereira, W.; Chapiro, G. Traveling Wave Solutions for Non-Newtonian Foam Flow in Porous Media. *Transp. Porous Media* **2023**, *148*, 247–265. [CrossRef]
20. Castrillón Vásquez, A.J.; Lozano, L.F.; Chapiro, G. The traveling foam wavefront in fractured porous medium. *J. Comput. Phys.* **2024**, *519*, 113437. [CrossRef]
21. Valdez, A.R.; Rocha, B.M.; da Fonseca Façanha, J.M.; de Souza, A.V.O.; Pérez-Gramatges, A.; Chapiro, G.; dos Santos, R.W. Foam-Assisted Water–Gas Flow Parameters: From Core-Flood Experiment to Uncertainty Quantification and Sensitivity Analysis. *Transp. Porous Media* **2022**, *144*, 189–209. [CrossRef]
22. Ribeiro, L.S.; Miranda, G.B.; Rocha, B.M.; Chapiro, G.; Weber dos Santos, R. On the Identifiability of Relative Permeability and Foam Displacement Parameters in Porous Media Flow. *Water Resour. Res.* **2024**, *60*, e2023WR036751. [CrossRef]
23. de Miranda, G.B.; dos Santos, R.W.; Chapiro, G.; Rocha, B.M. Uncertainty Quantification on Foam Modeling: The Interplay of Relative Permeability and Implicit-texture Foam Parameters. *Transp. Porous Media* **2025**, *152*, 8. [CrossRef]
24. de Moura Ribeiro, A.; Lopes, L.F.; Rocha, B.M.; Weber dos Santos, R.; Façanha, J.M.F.; Pérez-Gramatges, A.; Chapiro, G. Quantifying Experimental Impacts on Non-Newtonian Foam Characterization for Flow Modeling in Porous Media: Insights From Foam-Quality and Flow Rate Scan Experiments. *Water Resour. Res.* **2025**, *61*, e2024WR039536. [CrossRef]
25. Wang, J.; Hu, Y.; Chu, X.; Sun, G.; Lu, T. Roles and thresholds of viscosity and interfacial tension in surfactant flooding for residual oil recovery. *Front. Chem.* **2025**, *13*, 1660041. [CrossRef] [PubMed]
26. Tang, J.; Wei, B.; Yang, M.; Rossen, W.R. Critical Thresholds for CO2 Foam Generation in Homogeneous Porous Media. *SPE J.* **2025**, *30*, 439–454. [CrossRef]
27. Vavra, E.; Bai, C.; Puerto, M.; Ma, K.; Mateen, K.; Hirasaki, G.J.; Biswal, S.L. Effects of velocity on N2 and CO2 foam flow with in-situ capillary pressure measurements in a high-permeability homogeneous sandpack. *Sci. Rep.* **2023**, *13*, 10029. [CrossRef] [PubMed]
28. Vavra, E.; Bai, C.; Puerto, M.; Ma, K.; Mateen, K.; Hirasaki, G.J.; Biswal, S.L. Effects of Pressure Oscillations on Foam Transport in Porous Media. *Transp. Porous Media* **2025**, *152*, 48. [CrossRef]
29. Chapiro, G.; Quinelato, T.O.; Pereira, W.; dos Santos, R.W.; Zitha, P.L.J. On Mapping Local Foam Mobility in Porous Media from Computed Tomography Data. *SPE J.* **2024**, *29*, 6096–6107. [CrossRef]

Disclaimer/Publisher's Note: The statements, opinions and data contained in all publications are solely those of the individual author(s) and contributor(s) and not of MDPI and/or the editor(s). MDPI and/or the editor(s) disclaim responsibility for any injury to people or property resulting from any ideas, methods, instructions or products referred to in the content.